Polycrystalline Compound of Co²⁺-doped Zn₂SnO₄: Structural and Photoluminescent Properties

T. L. Alvarenga[a], S. S. Pedro[a], A. López[a], L. P. Sosman[a]* (ID)

[a]*Universidade do Estado do Rio de Janeiro, Instituto de Física, Rua São Francisco Xavier, 20550-900, Rio de Janeiro, RJ, Brasil.*

In this work, Zn_2SnO_4:Co^{2+} (0.1%) was obtained through a solid-state reaction at high temperature using ZnO, SnO_2, and $CoCO_3$. The sample was investigated using X-ray diffraction, X-ray fluorescence, scanning electron microscopy, and photoluminescence spectroscopy. Rietveld refinements of the X-ray diffraction data showed two crystalline phases, Zn_2SnO_4 and SnO_2, with proportions of 97.24% and 2.76%, respectively, while Zn and Sn atoms were observed by X-ray fluorescence. Scanning electron microscopy images showed the polycrystalline nature of the material. Photoluminescence spectroscopy showed two emission bands in the red and near-infrared regions, with the broader and more intense band having a barycenter at 694 nm. The intensity of the emission changed with the excitation wavelength, whereas the barycenter remained unchanged. The intensity, shape, and position of the bands, as well as the calculated crystal field parameters, indicate the insertion of Co^{2+} ions in the tetrahedral sites of the Zn_2SnO_4 material.

Keywords: *Photoluminescence, emission, Co^{2+}, Zn_2SnO_4.*

1. Introduction

ZnO, SnO_2, and $ZnO–SnO_2$ compounds have been investigated owing to their interesting properties. ZnO–SnO_2 materials are appropriate for applications such as photovoltaic solar cells and light emitting diodes (LEDS), piezoelectric devices, and antibacterial and antifungal activity[1–4], for example.

Among $ZnO–SnO_2$ compounds, Zn_2SnO_4 has properties that lead to its application in sensors[5], photocatalyst materials[6–8], persistent phosphorescence devices[9], lithium-ion battery electrodes[10], functional semiconducting materials with a wide direct band gap, and light emitting materials[11].

Zn_2SnO_4 has an inverse spinel structure, with an A_2BO_4[12] composition, in which A is a divalent cation and B is a trivalent or tetravalent cation. In this compound, Zn^{2+} cations occupy tetrahedral and octahedral sites, whereas Sn^{2+} cations are only in octahedral coordination.

Owing to its spinel structure, Zn_2SnO_4 can be used as a host for divalent cations with affinity to the tetrahedral sites, such as Co^{2+} and Mn^{2+} ions, and as a host for ions with affinity to the octahedral sites, such as Ni^{2+}. Zn_2SnO_4 can also be an appropriate host for ions with 4+ valence, such as Mn^{4+} ions in the octahedral site of the Sn^{4+} ions[13].

The properties of a material depend strongly on the synthesis method. Therefore, preparation processes are chosen in accordance with the desired properties. Beyond remarkable physical and chemical properties, factors such as a long useful life, environmental friendliness, and low financial costs are also important requirements for the production and use of functional materials. The solid-state method is appropriate for the preparation of many compounds with these

characteristics. For example, we investigated the compound $MgGa_2O_4$:Co^{2+} obtained through the solid-state method for the first time in 1992. More than two decades later, it was observed that the structural and photoluminescent properties of the $MgGa_2O_4$:Co^{2+} sample remained unchanged[14].

The high-temperature solid-state method consists of a reaction between raw materials at temperatures exceeding 1000 °C. The advantage of this method is that no solvent is used during the reaction, which makes preparation easier and avoids the insertion of contaminants into the mixture. However, the homogeneity and composition of the obtained samples are sometimes not fully satisfactory. Despite this, in the case of light-emitting materials for which a small impurity can lead to the quenching of luminescence, the solid-state method is a good sample preparation method. These characteristics encouraged the use of the solid-state method in this study.

Emissions from Zn_2SnO_4 samples produced by the solid-state method containing different kinds of impurities and different doping levels have been reported in the literature. Some are cited as follows.

A Zn_2SnO_4:Cr^{3+},Eu^{3+} material shows photoluminescence in the near-infrared region (with a maximum at 800 nm) attributed to the Cr^{3+} ions. The effect was significantly enhanced when Eu^{3+} ions were incorporated into the host owing to energy transfer processes from Eu^{3+} to Cr^{3+} ions[15].

Another example of an interesting emitting system is the undoped Zn_2SnO_4 powder obtained via a modified solid-state reaction method. In this process, the precursors are submitted to a high-energy milling process before the reaction. The material exhibits a photoluminescence emission band with a peak at 684 nm, which can be deconvoluted by

Gaussian fitting into four emission bands[16]. Another material of note is $Zn_{1+x}Ga_{2-2x}Sn_xO_4:Cr^{3+}$, which exhibits a long near-infrared afterglow when synthesized by high-temperature solid-state methods. The photoluminescent band, excited by a 365 nm LED, ranges from 600 to 900 nm and is composed of the R1, R2, N1, and N2 lines assigned to octahedrally coordinated Cr^{3+}[17].

Co^{2+} ions present interesting optical properties in different materials, as can be seen in the following examples. Dithiocarbamate nanowires containing Co(II) present an emission band from 455 to 526 nm due to the hexa-coordinated Co(II)[18]. Additionally, $Zn_2SiO_4:Co^{2+}$ presents a blue emission (peaks at 420 and 480 nm) and green emission (at 525 nm), showing a potential for use as blue and green phosphors for luminescent systems[19]. Finally, the mononuclear Co(II) complexes of substituted hydrazino quinoline Schiff bases exhibit an emission band from 434 to 465 nm, with high luminescence intensity, indicating a potential use as a novel material in organic LED technology[20].

The goals of this study were the production of Zn_2SnO_4 containing Co^{2+} as a substitutional impurity in Zn sites and the investigation of its structural and photoluminescent properties. $Zn_2SnO_4:Co^{2+}$ was obtained by a solid-state reaction at high temperature using ZnO, SnO_2, and $CoCO_3$ as precursors. The crystalline properties were determined from X-ray diffraction (XRD) data, which were refined by the Rietveld method using the FullProf program[21]. The morphology of the sample was observed using scanning electron microscopy (SEM), and the images were used to determine the size and shape of the grains. X-ray fluorescence (XRF) was used to verify the cation composition of the sample and to investigate the possibility of the presence of spurious species. Photoluminescence, excitation, and decay time measurements were performed to determine the emission characteristics of the sample. The measurements confirmed the production of an intense and broad band in the near-infrared region due to the insertion of Co^{2+} into the Zn_2SnO_4 host.

2. Materials and Methods

A sample with the molecular formula $Zn_{2(1-x)}Co_{2x}SnO_4$, where x = 0.001, was produced by a solid-state reaction using the raw materials ZnO, SnO_2, and $CoCO_3$. The quantities of the raw materials were calculated and weighed to produce 2 g of the desired compound according to the following stoichiometric reaction:

$$1.998 ZnO + 0.002 CoCO_3 + SnO_2 \rightarrow Zn_{1.998}Co_{0.002}SnO_4 + 0.002 CO_2 \quad (1)$$
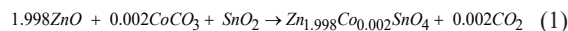
The mass of each raw material was obtained as follows. First, the molecular mass of each raw material was calculated using the atomic masses of its elements. The atomic mass

values used were Zn = 65.382, O = 15.999, Co = 58.933, C = 12.011, and Sn = 118.71, yielding:

$$1.998\, ZnO = 1.998\,(65.382+15.999) = 162.5960\,;$$

$$0.002\, CoCO_3 = 0.002\,(58.933+12.011+3\,x\,15.999) = 0.2378\,;$$

$$SnO_2 = 118.71+\,2\,x\,15.999 = 150.7088\,;$$

$$Zn_{1.998}Co_{0.002}SnO_4 = 1.998\,x\,65.382+0.002\,x\,58.933+118.71+4\,x\,15.999 = 313.4571\,.$$

Next, the quantities of raw materials to produce 2 g of $Zn_{1.998}Co_{0.002}SnO_4$ were calculated:

$$ZnO: \frac{162.5960}{313.4571} \times 2\text{ g} = 1.0374\text{ g} \quad (2)$$

$$SnO_2: \frac{150.7088}{313.4571} \times 2\text{ g} = 0.9616\text{ g} \quad (3)$$

$$CoCO_3: \frac{0.2378}{313.4571} \times 2\text{ g} = 0.0015\text{ g} \quad (4)$$

Table 1 lists the materials and quantities used in this study. The powders were then mixed with a pestle in a mortar made from agate for two hours.

Subsequently, the mixture was separated into three portions with similar masses, and each mixture was pressed under 296 MPa into a dish with a diameter of 13 mm and thickness of 2 mm. The dishes were then placed in an alumina crucible inside an electric oven at atmospheric pressure. The samples were heated to 1300 °C for 6 h. Finally, the furnace was turned off, and the samples cooled naturally to room temperature. Figure 1 shows a flowchart of sample preparation, and Figure 2 shows the sample preparation scheme.

In the stoichiometric reaction, the objective was the substitution of 0.1% of the Zn^{2+} ions of the host Zn_2SnO_4 by Co^{2+} ions. Therefore, the obtained sample was named $Zn_2SnO_4:Co^{2+}$ (0.1%).

One dish of the sample was crushed to a fine homogeneous powder, which was placed in a horizontal holder for XRD measurement. Powder XRD measurements were performed using a Bruker D2 PHASER powder diffractometer equipped with a Cu tube operating at 30 kV and 10 mA with X-ray Cu-Kα_1 radiation (1.5406 Å wavelength) at room temperature and scanning 2θ from 10° to 80° with steps of 0.01°.

The experimental results were refined using the Rietveld method with the FullProf package[21]. The diffracted peaks were fitted using a pseudo-Voigt profile function, and the pattern was compared to the Inorganic Crystal Structure Database (ICSD) patterns[22], with ICSD codes 028235 (Zn_2SnO_4) and 084576 (SnO_2). The Rietveld refinement of the X-ray data was used to obtain crystallographic parameters such as lattice

Table 1. Materials and quantities used for fabrication of $Zn_{1.998}Co_{0.002}SnO_4$ [$Zn_2SnO_4:Co^{2+}$ (0.1%)].

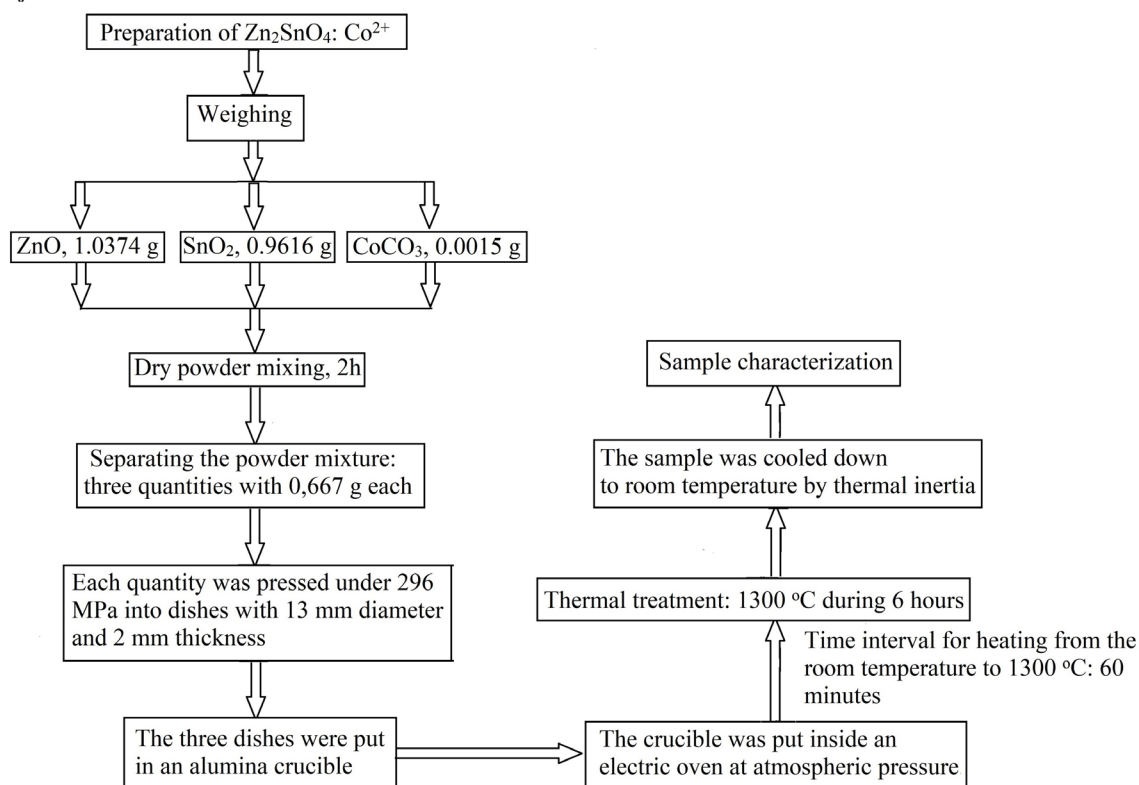| Raw Material	Brand Material	Purity (%)	Molecular Mass (g/mol)	Quantities for 2g of the sample (g)
ZnO	Carlo Erba	99.5	81.3794	1.0374
SnO$_2$	Aldrich Chemistry	99.9	150.7088	0.9616
CoCO$_3$	Colleman & Bell Co.	99.0	118.9420	0.0015

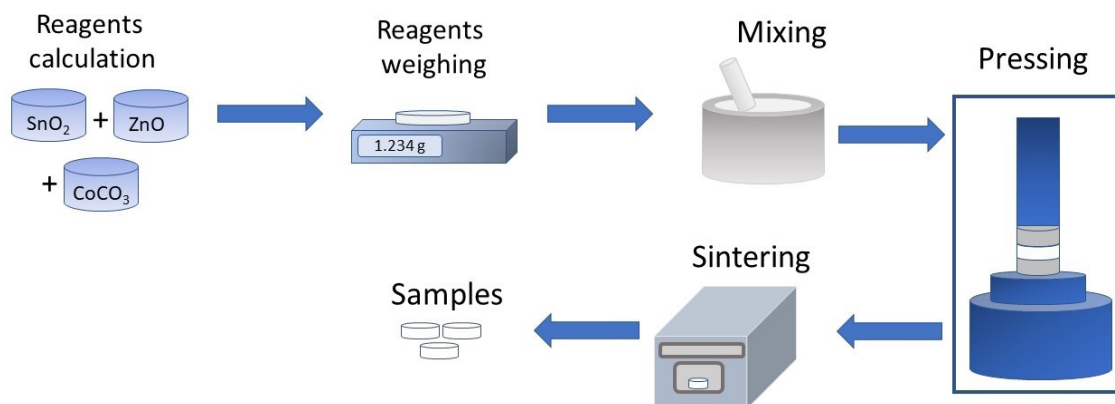**Figure 1.** Flowchart of sample preparation.

Figure 2. Diagram of the sample preparation steps.

parameters, space group, crystal system, cell volume, and phase quantities.

The elemental contents of the sample were identified using an Artax 200 XRF Spectrometer (30 kV, 400 µA, and molybdenum anode) with a silicon drift detector and a 400 µm beam spot. Measurements were performed at five distinct points on the sample surface to verify the homogeneity. All points showed the same results.

SEM images were obtained using an FEN Quanta 250 operating at 20 kV with magnifications of x7, x32,

x362, x846, x2539, and x2889. Because the sample is a hygroscopic material, one dish of the sample was dried in an oven at 100 °C for 20 h before SEM measurements, which were performed without any coating on the sample surface.

Photoluminescence, excitation, and emission decay time measurements were performed at room temperature using a PTI QuantaMaster 300-Plus spectrofluorometer. The radiation source was a pulsed 75 W xenon lamp with a frequency of 200 Hz. The modulation frequency corresponded to a 5 ms temporal window. In the measurements, 600 pulses were

averaged per wavelength, and the wavelength scan was performed with a 1 nm step size with detection performed by photon counting. A set of Newport optical filters was used to block the excitation light scattered inside the optical cavity and the room light. Figure 3 shows the measurements scheme.

The sample was first measured using XRD to verify the formation of the desired material, and Rietveld refinement was performed to determine the crystalline parameters, atomic positions, and phase quantities. Subsequently, photoluminescence and excitation measurements were performed to verify the possible emission from the sample. Next, SEM was used to verify the morphology, and XRF was finally performed to verify the atomic species in the sample. All measurements were performed at room temperature under ambient pressure.

3. Results

Figure 4 shows the room temperature XRD data and Rietveld refinement results for $Zn_2SnO_4:Co^{2+}$ (0.1%). The experimental data (I_{obs}) are represented by red circles fitted using a pseudo-Voigt mathematical function. The mathematical fitting (I_{calc}) is the black line passing through the red circles.

As can be seen in Figure 4, Rietveld refinement indicates the existence of two phases in the sample, represented by two sets of green vertical bars that denote Bragg positions for each phase. The phases of the sample are represented as follows: the first set (top) represents the Bragg positions of the Zn_2SnO_4 main phase, whereas the second set (bottom) represents the Bragg diffraction positions of the raw non-reacted SnO_2 oxide.

The difference (I_{obs}-I_{calc}) between the measured values and those obtained from the pseudo-Voigt mathematical function, fitted from the ICSD data[22], generated the bottom solid line. The crystallographic and Rietveld refinement parameters of $Zn_2SnO_4:Co^{2+}$ (0.1%) are shown in Table 2, and the atomic positions are shown in Table 3. Zn_2SnO_4 belongs to the cubic crystal system with space group $Fd\overline{3}m$. It is described as an inverse spinel, where the tetrahedral sites are occupied by Zn2+ atoms [ZnO4] and the octahedral sites are occupied by both Zn2+ and Sn4+ atoms, [ZnO6] and [SnO6], respectively 12,13. Table 3 shows the uncertainty in the O1 position, which is due to the refinement of this position, while the positions Zn1, Zn2, and Sn1 were fixed. The observed secondary phase SnO2 is a quantity of the unreacted raw material. No quantity of the ZnO raw materials was observed in the XRD data.

Figure 5 shows XRF for $Zn_2SnO_4:Co^{2+}$ (0.1%) at room temperature. The observed peaks are related to the Zn and Sn atoms. The homogeneity of the sample was confirmed by performing the measurements in several regions on the sample's surface and obtaining similar results: only Zn and Sn atoms were observed. The lack of a Co^{2+} signal is due to the low concentration of this species in the sample, below the instrumental sensitivity.

Figure 6 shows SEM images obtained with 20 kV at magnifications of (a) x7, (b) x32, (c) x362, (d) x846, (e) x2539, and (f) x2889. These images show the polycrystalline characteristic of the sample, with angular Zn_2SnO_4 grains. A variation in particle size can also be seen.
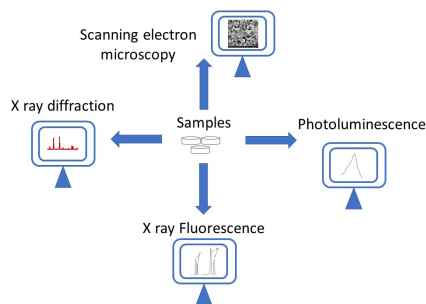
Figure 3. Simplified experimental scheme used for the $Zn_2SnO_4:Co^{2+}$ investigation.
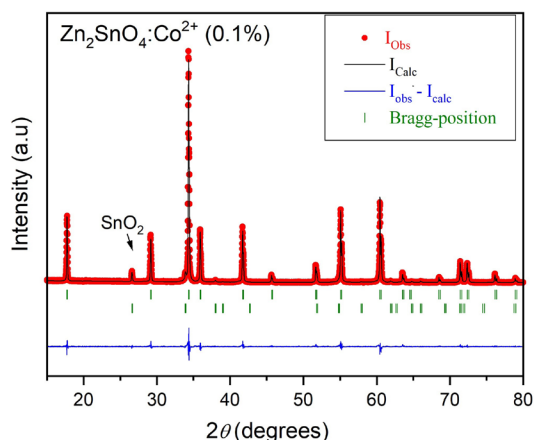
Figure 4. X-ray diffraction and Rietveld refinement data for the Zn2SnO4:Co²⁺ (0.1%) sample.

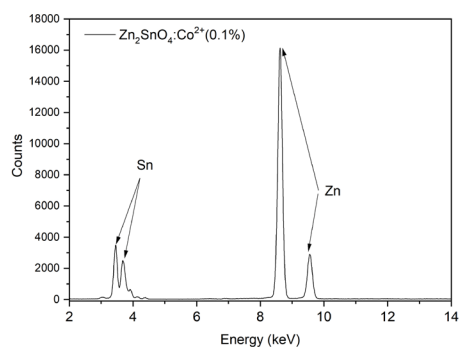**Table 2.** Crystallographic and Rietveld refinement parameters for $Zn_2SnO_4:Co^{2+}$ (0.1%) sample.

Phase	Zn_2SnO_4	SnO_2
ICSD #	28235	84576
Proportion (%)	97.24	2.76
Space group	$Fd\overline{3}m$	$P4_2/mnm$
Crystal system	*Cubic*	*Tetragonal*
a (Å)	8.656(5)	4.736(3)
b (Å)	-	-
c (Å)	-	3.185(5)
V(Å³)	648.69	71.46
Agreement factors		
R_{wp} = 13.1, R_p = 13.0, R_{exp} = 9.3,		
GOF = 1.4 and χ^2 = 1.96		

Table 3. Atomic positions obtained from Rietveld refinements.

Atom	Ox State	Wyck Symb	x	y	z
Zn1	2	8b	0.375	0.375	0.375
Zn2	2	16 c	0.000	0.000	0.000
Sn1	4	16 c	0.000	0.000	0.000
O1	-2	32 e	0.242(2)	0.242(2)	0.242(2)

Figure 7 shows the photoluminescence spectra of Zn_2SnO_4:Co^{2+} (0.1%) at room temperature, performed using excitation radiation wavelengths of 500, 530, 550, 600, and 620 nm. An optical filter was used in front of the luminescence detector to cut off wavelengths below 650 nm and block the excitation light and the radiation scattered in the optical cavity.

In the photoluminescence spectra (Figure 7), a broad homogeneous band from 650 to 750 nm, with a barycenter at 694 nm (14409 cm⁻¹), was observed. The emissions excited with 620 and 600 nm incident light are three times more intense than those excited with 550 nm light and twelve times more intense than those excited with 500 and 530 nm light.

In Figure 8, the room temperature emissions in the infrared region range from 790 to 900 nm. The emission with maximum intensity located at 851 nm (11750 cm⁻¹) was excited with wavelengths of 550, 600, and 620 nm. This band was not observed when other excitation wavelengths were used. Comparing Figure 7 and 8, the emission at 694 nm is more than 10 times more intense than that at 851 nm.

Fig. 9 presents the excitation spectrum of the sample at room temperature. The excitation spectrum of Zn_2SnO_4:Co^{2+} (0.1%) was monitored at 705 nm. The emission wavelength position (705 nm), a few nanometers out of the band barycenter (694 nm), was chosen to allow the observation of the greatest number of transitions in the visible region.
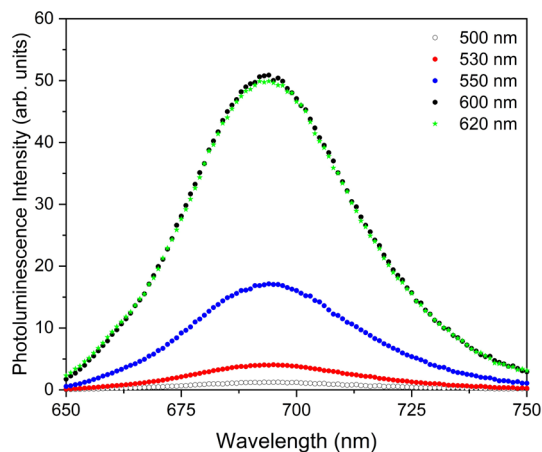
Room temperature photoluminescence decay measurements of Zn_2SnO_4:Co^{2+} (0.1%) are shown in Figure 10. The decay time was monitored at emission wavelengths of 692 and 850 nm. Both measurements were performed with a wavelength excitation (λ_{ex}) of 640 nm. For the 692 nm wavelength, the decay time is ~10.4 μs, and for the 850 nm wavelength, the decay time is ~8.7 μs.

4. Discussion

The XRD measurements and Rietveld refinement results (Figure 4) are listed in Tables 2 and 3. The refinement quality is estimated by the goodness of fit (GOF) index, which indicates whether the crystalline parameter values obtained from refinement of the X-ray data agree with those described in the literature. The GOF index for a good fit is close to 1.0 [21]. The obtained value for the GOF-index
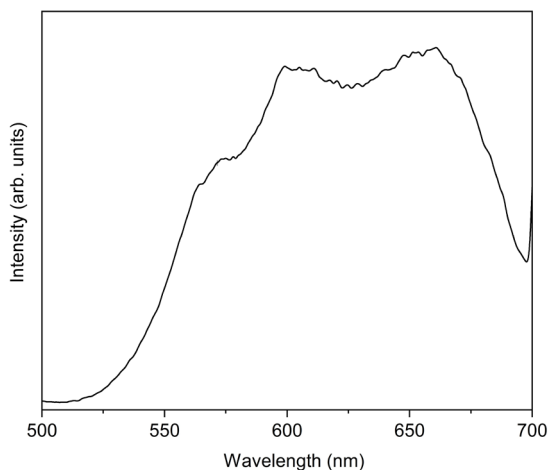
Figure 5. X-ray fluorescence (XRF) for Zn_2SnO_4:Co^{2+} (0.1%) at room temperature.
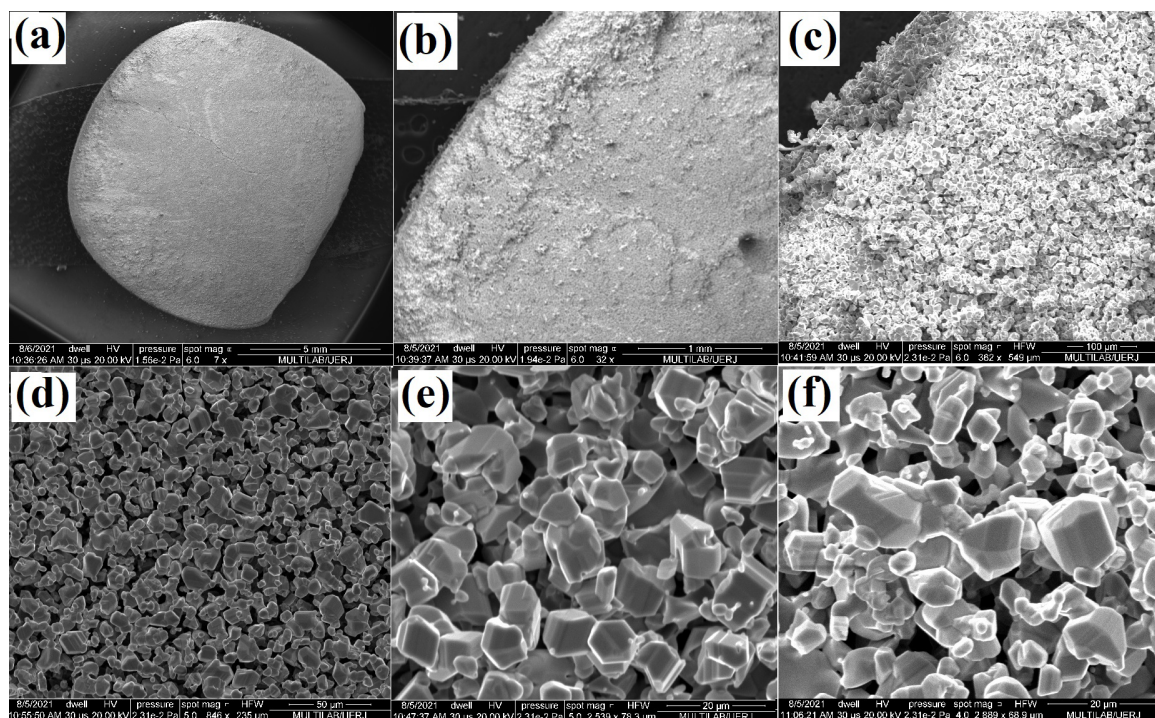
Figure 6. Scanning electronic microscopy (SEM) images of Zn_2SnO_4:Co^{2+} (0.1%), with magnifications of (a) x7, (b) x32, (c) x362, (d) x846, (e) x2539, and (f) x2889.
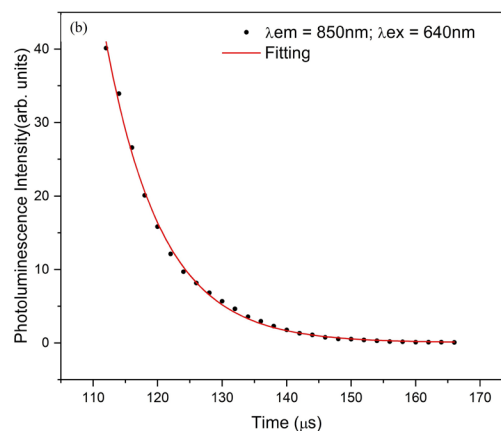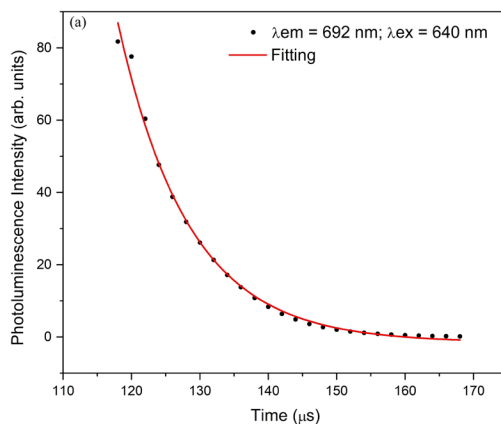
Figure 7. Room temperature photoluminescence spectra of Zn_2SnO_4:Co^{2+} (0.1%).
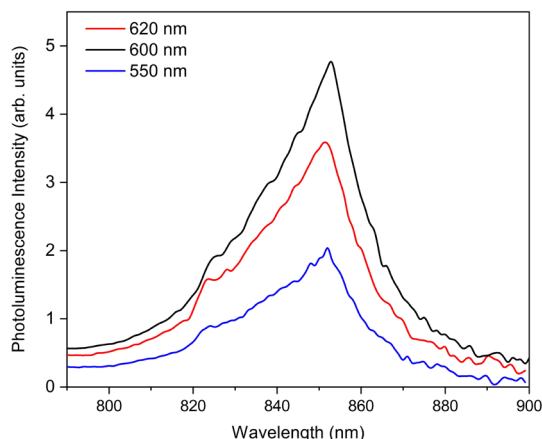
Figure 8. Near infrared room temperature photoluminescence spectra of Zn_2SnO_4:Co^{2+} (0.1%).

Figure 9. Room temperature excitation spectrum of the Zn_2SnO_4:Co^{2+} (0.1%) monitored at 705 nm.

Figure 10. Room temperature photoluminescence decay measurements of the Zn_2SnO_4:Co^{2+} (0.1%) monitored at (a)λ_{em}=692 nm and (b) λ_{em}=850 nm.

refinement in this study was 1.4, which indicates a correct structural characterization.

The XRD pattern shows two phases in the sample: Zn_2SnO_4 and SnO_2. Rietveld refinement results determined percentages of 97.24% and 2.76% of the total mass of the sample for Zn_2SnO_4 and SnO_2, respectively.

The small quantity of unreacted SnO_2 might be explained by one of two phenomena: a)first, it was necessary to thermally treat the Zn_2SnO_4 at high temperature for several hours. This procedure can cause mass loss of species that have high volatility, such as the Zn atoms. This loss could have resulted in some quantity of unreacted raw material and/or formation of undesired phases. b) the hygroscopic characteristics of the raw oxides ZnO and SnO_2. This point is discussed in the next paragraph.

Alternatively, the unreacted SnO_2 may be due to the significant hygroscopic behavior of ZnO, which is much greater than that of SnO_2[23,24]. Because of the hygroscopic character of ZnO, it is expected that its quantity in the ZnO–SnO_2 mixture is lower than that necessary for a complete reaction with SnO_2, since some water quantity is added to the ZnO mass. It is important to point out that this hypothesis is possible

only if the amount of water adsorbed in ZnO is measurable. In other words, the quantity of water adsorbed by ZnO leads to a deficit of ZnO during the reaction because the weighed mass includes both ZnO and H_2O. SnO_2 is also hygroscopic; therefore, the SnO_2 quantity is also lower than that necessary for a stoichiometric reaction because the mass included both SnO_2 and H_2O. However, as SnO_2 is less hygroscopic than ZnO, the relative quantity of H_2O in SnO_2 is expected to be lower than that in ZnO. As a consequence of the volatility and higroscopy, no quantity of ZnO remained in the sample, and only a small quantity of unreacted SnO_2 beyond the main phase Zn_2SnO_4 was observed in the XRD data.

Table 3 shows the atomic positions of the Zn, Sn, and O atoms in the Zn_2SnO_4 host obtained from the Rietveld refinements. The Zn^{2+} ions are in two types of sites: Zn1 in the 8a-Wyckoff position (tetrahedral symmetry) and Zn2 in the 16d-Wyckoff position (octahedral symmetry), both coordinated by O^{2-} ions. Sn^{4+} ions are in the 16d-Wyckoff position, with the same atomic coordinates as octahedral Zn2 ions. Therefore, Zn2 and Sn ions have a common position in the host. Because the amount of SnO_2 is small, the intensity of the Bragg peaks is low. Therefore, it was not possible to perform refinements in the atomic parameters of this phase.

The main characteristics that must be observed for an ion inserted as a substitutional impurity in a host crystal are similarities between the valences and between the ionic radii of the host ion and the substitutional ion. When the valence states are considered, the $Co^{2+} \rightarrow Sn^{4+}$ substitution in the host Zn_2SnO_4 implies a rearrangement of the host ions because of the difference between the Co^{2+} and Sn^{4+} valences. Therefore, the probability of the substitution of $Co^{2+} \rightarrow Zn^{2+}$ sites is higher because, in this case, no charge compensation or a remarkable atomic rearrangement would be necessary. Therefore, the substitution of Zn^{2+} by Co^{2+} ions is more favorable than that of Sn^{4+} by Co^{2+} ions.

The second important characteristic is the ionic radii. The ionic radii of Co^{2+}, Zn^{2+}, and Sn^{4+} in tetrahedral coordination are equal to 0.58, 0.60, and 0.55 Å, respectively, whereas in octahedral coordination they are 0.65, 0.74, and 0.69 Å, respectively[25]. Ions of similar sizes to host ions are typically easier to substitute. Therefore, considering the ionic radii, the substitution of Zn^{2+} by Co^{2+} ions in tetrahedral coordination is easier than the substitution of Sn^{4+} by Co^{2+} ions. On the other hand, in octahedral sites, the Sn^{4+} substitution by Co^{2+} ions would be more favorable.

Hautier et al. proposed in reference[26] a probabilistic model of ionic species substitution without remarkable crystal structure changes. In this work, the authors defined the parameter "pair correlation": two ions that substitute each other easily have a pair correlation higher than 1. The highest pair correlation value presented by the authors was equal to 9.77 for Cd^{2+}–Fe^{2+} substitution. The Co^{2+}–Zn^{2+} substitution pair correlation was the third highest value, 9.57, while the pair correlation value for Co^{2+}–Sn^{4+} substitution was 3.75 (rank 247). These pair correlation values indicate that the Zn^{2+} ions are more substitutable by Co^{2+} ions than the Sn^{4+} ions.

From the low probability of $Co^{2+} \rightarrow Sn^{4+}$ substitution, as well as the small quantity of SnO_2 in the sample, the

photoluminescence can be considered a result only of Co^{2+} in the Zn^{2+} sites of Zn_2SnO_4.

The XRF of Zn_2SnO_4:Co^{2+} (0.1%) at room temperature is shown in Figure 5. In this figure, the intensity of the Zn peaks is higher than that from Sn atoms. XRF is a quantitative technique in which the intensity of the generated X-rays depends on the concentration of the species in the sample. Therefore, the XRF measurements confirm that the number of Zn atoms is higher than that of Sn atoms, as expected.

Figure 6 shows the SEM images of the sample. Figure 6a shows a full view of the sample and dish with a fracture caused by manipulation. Figs. 6b, c show that the surface is irregular, but the grains are not visible. Figure 6d shows a characteristic polycrystalline sample with a porous microstructure. In Figure 6e, f, the angular grains have a size distribution ranging from 1 to 10 μm. In Figure 6f, the angular grains were associated with Zn_2SnO_4, and the smaller smooth-faced grains with a size of ~ 1 μm were associated with SnO_2[27].

In the photoluminescence spectra (Figure 7), a broad, homogeneous band from 650 to 750 nm, with a barycenter at 694 nm, was observed. The emissions excited with 620 and 600 nm light are three times more intense than the emission excited with 550 nm light and twelve times more intense than the emissions excited with 500 and 530 nm light. This result is the first indication that the emission with barycenter at 694 nm can be attributed to Co^{2+} in tetrahedral sites, because red radiation is strongly absorbed by Co^{2+} ions, which suggests emission from the tetrahedrally coordinated Co^{2+}[27-30]. In addition, the observed emission band has a shape and wavelength position similar to emissions from tetrahedrally coordinated Co^{2+}.

The tetrahedral sites occupied by Co^{2+} ions do not have exactly the same characteristics. For example, the Co^{2+}–O^{-2} distance varies, the Co^{2+} sites have distortions, and the crystal field strength depends on the ligand–impurity distance and symmetry of the occupation site, among other things. Therefore, each Co^{2+} ion is subjected to a specific crystalline field strength. Most of the energy levels of transition metal ions, such as the Co^{2+} ion, are strongly affected by the crystalline field strength. This effect leads to a variation in the energy gap between the fundamental level and excited emitting level. Consequently, each excited Co^{2+} ion decays to the fundamental level with a different energy, which depends on the crystal field strength. This variability of the emission energies leads to the broad band observed in Figure 7. In addition, high-intensity emission bands are characteristic of spin-allowed transitions, which occur between energy levels with the same spin multiplicity.

From the Tanabe–Sugano diagrams[31], the d^7 electronic configuration in tetrahedral symmetry is equivalent to the d^3 electronic configuration in octahedral sites. The fundamental energy level ^4F splits into three energy levels: the ground $^4A_2(^4F)$ and excited levels $^4T_2(^4F)$ and $^4T_1(^4F)$. The excited ^4P energy level transforms into the $^4T_1(^4P)$ energy level, and the ^2G level splits into the $^2A_1(^2G)$, $^2T_1(^2G)$, $^2T_2(^2G)$, and $^2E(^2G)$ excited energy levels. A transition in the visible and infrared regions of d^7 configuration ions (such as the Co^{2+} ion) in tetrahedral sites occurs among the ^4P and ^4F states[30]. The excited energy levels originating from the ^4P and ^4F states

have the same spin multiplicity and a strong dependence on the crystal field strength[30], thus generating broad and intense bands. Therefore, the emission at 694 nm (14,409 cm^{-1}) was assigned to the $^4T_1(^4P) \rightarrow ^4A_2(^4F)$ transition of the Co^{2+} ion with tetrahedral symmetry.

Figure 8 shows the emission in the infrared region from 790 to 900 nm. The emission with the maximum intensity located at 851 nm (11750 cm^{-1}) was excited with wavelengths of 550, 600, and 620 nm. This band was not observed when other excitation wavelengths were used.

The band in Figure 8 is associated with the $^4T_1(^4P) \rightarrow ^4T_2(^4F)$ spin-allowed electronic transition of Co^{2+} in tetrahedral coordination. The intensity of this band is ten times weaker than the intensity of the maximum emission band with barycenter at 694 nm (Figure 7). This occurs because the non-radiative decay processes in the infrared region are more competitive than those in the visible region. Therefore, in general, the infrared bands are weaker than those in the visible region.

Using the energies of the $^4T_1(^4P) \rightarrow ^4A_2(^4F)$ (14,409 cm^{-1}) and $^4T_1(^4P) \rightarrow ^4T_2(^4F)$ (11,750 cm^{-1}) emissions in the Tanabe–Sugano matrices[30,31], as described in detail in reference[20], the energy parameters were calculated: crystal field strength Dq = 266 cm^{-1}, and interelectronic energy (Racah parameters) B = 783 cm^{-1} and C = 3524 cm^{-1}.

For the free Co^{2+} ion, B = 971 cm^{-1}[31–32], so in Zn_2SnO_4, this energy parameter is reduced by ~20% of the free ion value. This reduction in the Racah parameter B indicates a covalent character in the Co^{2+}–O^{2-} bond.

Figure 9 shows the excitation spectrum of the sample at room temperature. This measurement was performed to identify the excited energy levels of Zn_2SnO_4:Co^{2+}, to determine which wavelength is most appropriate for achieving emission with an intensity as high as possible and to investigate the presence of spurious impurities. The excitation spectrum of Zn_2SnO_4:Co^{2+} (0.1%) was obtained by setting the wavelength to 705 nm, which was continuously excited with wavelengths from 500 to 700 nm. This emission wavelength position, a few nanometers from the band barycenter (694 nm), was chosen to allow the observation of the greatest possible number of transitions in the visible region. The spectrum is similar to the results observed for tetrahedrally coordinated Co^{2+} in other materials[27–29]. From the Tanabe–Sugano diagram[31], these bands were attributed to the spin-forbidden transitions $^4A_2(^4F) \rightarrow ^2A_1(^2G)$ at 574 nm (17421 cm^{-1}) and $^4A_2(^4F) \rightarrow ^2E(^2G)$ at 602 nm (16611 cm^{-1}), and to the spin-allowed transition $^4A_2(^4F) \rightarrow ^4T_1(^4P)$ at 657 nm (15220 cm^{-1}). The excitation

spectrum agrees with the photoluminescence data, because in Figure 7 and 8 the intensity is enhanced with excitation at 620 and 600 nm, respectively. Table 4 shows the energy transitions and energy parameters of Zn_2SnO_4:Co^{2+} (0.1%).

Figure 10 presents the decay time curves of the photoluminescence of Zn_2SnO_4:Co^{2+} (0.1%) at room temperature. The decay starts at 110 μs, just after the lamp is turned off. The obtained short lifetime, approximately 10 μs for both measurements, is characteristic of spin-allowed transitions, such as those associated in this paper with tetrahedrally coordinated Co^{2+}.

The curves have an exponential decay profile, indicating the dominant radiative character of the decay processes. It was also observed that the decay time of the emission at 850 nm was shorter than that at 692 nm. It is known that non-radiative decay has a shorter lifetime than radiative decay. Therefore, the weakness of the band at 850 nm, as well as the difference between the decay times, could be explained by the non-radiative processes contributing to the relaxation of the $^4T_1(^4P)$ energy level.

Figure 11 shows the energy levels and transitions of Co^{2+} ions. The energy processes can be described as follows: (a) Co^{2+} ions were excited from the $^4A_2(^4F)$ fundamental energy level to the $^2A_1(^2G)$, $^2E(^2G)$, and $^4T_1(^4P)$ excited levels. From the $^2A_1(^2G)$ and $^2E(^2G)$ levels, the Co^{2+} ions decay by non-radiative processes to the $^4T_1(^4P)$ and $^4T_2(^4F)$ energy levels. At the $^4T_1(^4P)$ level, Co^{2+} ion relaxation occurs through radiative processes to the fundamental level $^4A_2(^4F)$ and to the excited $^4T_2(^4F)$ level.

A part of the energy absorbed by Co^{2+} ions leading the system to the $^4T_1(^4P)$ state is released by non-radiative processes such as vibrational energy transfer. Moreover, some Co^{2+} ions at the highest vibration level inside the $^4T_1(^4P)$ electronic energy level decay to the lowest vibrational sublevel inside the $^4T_1(^4P)$ level. Therefore, photoluminescence occurs from the lowest vibrational level of $^4T_1(^4P)$ to $^4A_2(^4F)$ and $^4T_2(^4F)$. The difference between the excitation and emission energies of $^4T_1(^4P) \rightarrow ^4A_2(^4F)$ (Stokes shift) was 812 cm^{-1}. This value reflects the partial overlap between the excitation and emission bands, as observed in Figure 7 and 9, which leads to some loss of intensity in the emission band.

As mentioned in the Introduction section, the undoped Zn_2SnO_4 presents an inhomogeneous broad emission band from 500 to 800 nm with a peak intensity at 684 nm[16]. This band was deconvoluted in four Gaussian curves with barycenters at 563.5, 626.1, 688.8, and 738.0 nm. The authors attributed these emissions to trapped states due to oxygen vacancies,

Table 4. Energy transitions and parameters for Zn_2SnO_4:Co^{2+} (0.1%).

Transition (excitation)	Wavelength (nm)	Energy (cm^{-1})
$^4A_2(^4F) \rightarrow ^2A_1(^2G)$	574	17421
$^4A_2(^4F) \rightarrow ^2E(^2G)$	602	16611
$^4A_2(^4F) \rightarrow ^4T_1(^4P)$	657	15220
Transition (emission)	Wavelength (nm)	Energy (cm^{-1})
$^4T_1(^4P) \rightarrow ^4A_2(^4F)$	694	14409
$^4T_1(^4P) \rightarrow ^4T_2(^4F)$	851	11750

Energy parameters: Dq = 266 cm^{-1}, B = 783 cm^{-1} and C = 3524 cm^{-1}.
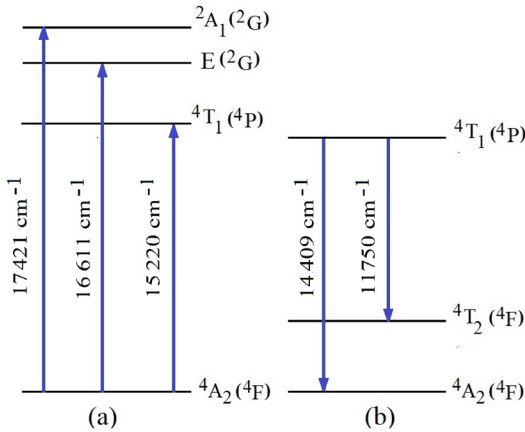
Figure 11. Energy levels and transitions of the Co²⁺ ion in tetrahedral site.

Zn/Sn vacancies, defects in the Zn/Sn stoichiometry, and point defects arising from the sample preparation method [16].

The highest energy emission band observed in this study (Figure 7) is homogeneous, with a wavelength interval from 650 to 750 nm and a barycenter at 694 nm. Comparing the Zn_2SnO_4[16] emission with Figure 7, the shapes and energy positions are not similar. Therefore, it is possible to state that the emission observed in this study was not due to the Zn_2SnO_4 host.

However, the results presented in this paper are similar to those observed for other samples obtained by the solid-state method, as follows.

Photoluminescence measurements of Zn_2TiO_4:Co²⁺ at room temperature[29] showed a broad, intense, and homogeneous band from 675 to 750 nm, with a barycenter at 714 nm when the sample was excited with 630 nm light. The energy parameters obtained from the spectra were Dq = 188 cm⁻¹, B = 808 cm⁻¹, and C = 3636 cm⁻¹, with Dq/B = 0.23. These values are characteristic of Co²⁺ in tetrahedral sites with some degree of covalence. Photoluminescence results obtained for Mg_2SnO_4:Co²⁺ at room temperature[33] showed a broad and intense band from 650 to 775 nm. The barycenter of the emission band shifted to a lower wavelength (from 692 to 698 nm) as the excitation wavelength decreased (from 640 to 500 nm). The energy parameters obtained were Dq = 270 cm⁻¹, B = 782 cm⁻¹, and C = 3519 cm⁻¹, with Dq/B = 0.35, which are characteristic of Co²⁺ ions in tetrahedral sites with a more ionic than covalent Co²⁺–O⁻² bond.

From the results presented above, it is reasonable to believe that the intensity of the emission from the Co²⁺ ion is high enough to hide the observation of the Zn_2SnO_4 host emission. Therefore, the photoluminescence of Zn_2SnO_4:Co²⁺ (0.1%) is due to Co²⁺ in the tetrahedral Zn sites.

5. Conclusions

From the Rietveld results, it can be concluded that the Zn_2SnO_4:Co²⁺ (0.1%) sample was formed as proposed in this study. The sample was fabricated using the solid-state method. The raw materials were manually mixed for 2 h,

followed shortly by a thermal treatment (6 h at 1300 °C). XRF measurements showed that Zn and Sn cations were homogeneously distributed in the sample and that no spurious species were detected. SEM measurements showed the polycrystalline characteristics of the sample, with grain sizes ranging from 1 to 10 μm.

The photoluminescence spectra of Zn_2SnO_4:Co²⁺ (0.1%) measured at room temperature were attributed to the ⁴T₁(⁴P) → ⁴A₂(⁴F) and ⁴T₁(⁴P) → ⁴T₂(⁴F) transitions, with barycenters at 694 and 851 nm, respectively. Both bands were attributed to Co²⁺ ions in the tetrahedral sites. The transitions between energy levels are strongly dependent on the crystal field strength, which leads to broad bands. Moreover, the spin-allowed electronic transitions are associated with intense bands, as observed in this study. The band at 694 nm is more intense than the band at 851 nm because the excited levels decay through competitive non-radiative processes in the infrared region more than in the visible region. The spectra do not show any evidence of spurious impurities. The luminescence decay lifetimes are characteristic of the emissions from tetrahedrally coordinated Co²⁺.

In the excitation spectra, we identified the spin-forbidden transitions ⁴A₂(⁴F) → ²A₁(²G) (574 nm) and ⁴A₂(⁴F) → ²E(²G) (602 nm), as well as the spin-allowed transition ⁴A₂(⁴F) → ⁴T₁(⁴P) (657 nm). From the spectra, and using the Tanabe–Sugano matrices, the crystal field Dq = 266 cm⁻¹ and Racah parameters B = 783 cm⁻¹ and C = 3524 cm⁻¹ were obtained (Dq/B ≈ 0.34). The Dq and Dq/B values are characteristics of the Co²⁺ ion in tetrahedral sites, while the B parameter indicates a covalent character for the Co²⁺–O⁻² bond. In this work, the most important results were the relatively simple sample production process and the observation of an intense and broad emission band.

6. Acknowledgments

7. References

1. Abdallah B, Kakhia M, Zetoun W, Alkafri N. PbS doped ZnO nanowires films synthesis by thermal evaporation method: Morphological, structural, and optical properties. Microelectronics J. 2021;111:105045. http://dx.doi.org/10.1016/j.mejo.2021.105045:105045.

2. Abdallah B, Kakhia M, Obaide A. Morphological and structural studies of ZnO nanotube films using thermal evaporation technique. Plasmonics. 2021;16(5):1549-56. http://dx.doi.org/10.1007/s11468-021-01420-x.

3. Abdallah B, Jazmati AK, Nounou F. Morphological, structural and photoresponse characterization of ZnO nanostructure

films deposited on plasma etched silicon substrates. Journal of Nanostructures. 2020;10(1):185-97.

4. Abdallah B, Jazmati AK, Kakhia M. Physical, optical and sensing properties of sprayed zinc doped tin oxide films. Optik. 2018;158:1113-22. http://dx.doi.org/10.1016/j.ijleo.2018.01.008.

5. Dazai T, Yasui S, Taniyama T, Itoh M. Bandgap tuning and optimization of green-emitting Zn_2SnO_4-Mg_2SnO_4:Mn^{2+} using combinatorial pulsed laser deposition. Ceram Int. 2020;46(13):21771-4. http://dx.doi.org/10.1016/j.ceramint.2020.05.288.

6. Thien ND, Vu LV, Long NN. The effect of interaction between surface plasmons of gold nanoparticles and optical active centers on luminescence of Eu^{3+}-doped Zn_2SnO_4 nanocrystals. Opt Mater. 2018;78:319-24. http://dx.doi.org/10.1016/j.optmat.2018.02.039.

7. Foletto EL, Simões JM, Mazutti MA, Jahn SL, Muller EI, Pereira LSF, et al. Application of Zn_2SnO_4 photocatalyst prepared by microwave-assisted hydrothermal route in the degradation of organic pollutant under sunlight. Ceram Int. 2013;39(4):4569-74. http://dx.doi.org/10.1016/j.ceramint.2012.11.053.

8. Zhou RL, Kong XY. Photoluminescence and characterization of ZnO/Zn_2SnO_4 nanocables. J Inorg Mater. 2011;26(6):597-601. http://dx.doi.org/10.3724/SP.J.1077.2011.00597.

9. Taktak O, Souissi H, Kammoun S. Optical properties of the phosphors Zn_2SnO_4:Cr^{3+} with near-infrared long-persistence phosphorescence for bio-imaging applications. J Lumin. 2020;228. http://dx.doi.org/10.1016/j.jlumin.2020.117563:117563.

10. Rong A, Gao XP, Li GR, Yan TY, Zhu HY, Qu JQ, et al. Hydrothermal synthesis of Zn_2SnO_4 as anode materials for Li-ion battery. J Phys Chem B. 2006;110(30):14754-60. http://dx.doi.org/10.1021/jp062875r.

11. Tsai MT, Chang YS, Liu YC. Photocatalysis and luminescence properties of zinc stannate oxides. Ceram Int. 2017;43:S428-34. http://dx.doi.org/10.1016/j.ceramint.2017.05.251.

12. Sickafus KE, Wills JM, Grimes NW. Structure of spinel. J Am Ceram Soc. 1999;82(12):3279-92. http://dx.doi.org/10.1111/j.1151-2916.1999.tb02241.x.

13. Grimes NW, Thompson P, Kay HF. New symmetry and structure for spinel. Proc R Soc Lond A Math Phys Sci. 1791;1983(386):333-45. http://dx.doi.org/10.1098/rspa.1983.0039.

14. Pedro SS, Silva MAFM, López A, Sosman LP. Structural and photoluminescent properties of the $MgGa_2O_4$:Co^{2+} ceramic compound revisited after two decades. Journal of Advanced Ceramics. 2015;4(4):267-71. http://dx.doi.org/10.1007/s40145-015-0160-2.

15. Zhang Y, Huang R, Lin Z, Song J, Wang X, Guo Y, et al. Co-dopant influence on near-infrared luminescence properties of Zn_2SnO_4:Cr^{3+},Eu^{3+} ceramic discs. J Alloys Compd. 2016;686:407-12. http://dx.doi.org/10.1016/j.jallcom.2016.06.041.

16. Vien LTT, Tu N, Tran MT, Van Du N, Nguyen DH, Viet DX, et al. A new far-red emission from Zn_2SnO_4 powder synthesized by modified solid state reaction method. Opt Mater. 2020;100:109670. http://dx.doi.org/10.1016/j.optmat.2020.109670:109670.

17. Pan Z, Castaing V, Yan L, Zhang L, Zhang C, et al. Facilitating low-energy activation in the near-infrared long-afterglow complex spinel Zn1+xGa2−2xSnxO4:Cr3+ via band gap engineering and control of cation occupancy. J Phys Chem C. 2020;124(15):8347-58

18. Ujjain KS, Ahuja P, Sharma RK, Singh G. Synthesis, electronic and optical properties of cobalt (II) Dithiocarbamate fluorescent

19. Rasdi NM, Fen YW, Azis RS, Omar NAS. Photoluminescence studies of cobalt (II) doped zinc silicate nanophosphors prepared via sol-gel method. Optik. 2017;149:409-15. http://dx.doi.org/10.1016/j.ijleo.2017.09.073.

20. Priyadarshini GS, Selvi G. Luminescence cobalt (II) complexes: synthesis, characterization, photophysical and DFT study. Materials Today: Proceedings. 2020;2020(40):S19-27. http://dx.doi.org/10.1016/j.matpr.2020.03.252.

21. FullProf Suite [homepage on the Internet]. The FullProf Team; 2006 [cited 2021 May 20]. Available from: https://www.ill.eu/sites/fullprof/index.html.

22. ICSD: Inorganic Crystal Structure Database [homepage on the Internet]. Collection code #28235. FIZ Karlsruhe; 2002 [cited 2021 May 20]. Available from: https://icsd.products.fiz-karlsruhe.de/.

23. Riza MA, Go YI, Maier RRJ, Harun SW, Anas SB. Hygroscopic materials and characterization techniques for fiber sensing applications: a review. Sens Mater. 2020;32(11):3755-72. http://dx.doi.org/10.18494/SAM.2020.2967.

24. Kam M, Zhang Q, Zhang D, Fan Z. Room-temperature sputtered SnO_2 as robust electron transport layer for air-stable and efficient perovskite solar cells on rigid and flexible substrates. Sci Rep. 2019;9(1):6963. http://dx.doi.org/10.1038/s41598-019-42962-9.

25. Shannon RD. Revised effective ionic radii and systematic studies of interatomic distances in halides and chalcogenides. Acta Crystallogr A. 1976;32(5):751-67. http://dx.doi.org/10.1107/S0567739476001551.

26. Hautier G, Fischer C, Ehrlacher V, Jain A, Ceder G. Data mined ionic substitutions for the discovery of new compounds. Inorg Chem. 2011;50(2):656-63. http://dx.doi.org/10.1021/ic102031h.

27. Zang GZ, Wang XF, Li LB, Guo HF, Chen QD. Sintering and varistor behaviour of SnO_2-Zn_2SnO_4 composite ceramics. J Electroceram. 2013;31(1-2):134-7. http://dx.doi.org/10.1021/ic102031h.

28. Kuleshov NV, Mikhailov VP, Scherbitsky VG, Prokoshin PV, Yumashev KV. Absorption and luminescence of tetrahedral Co^{2+} ion in $MgAl_2O_4$. J Lumin. 1993;55(5-6):265-9. http://dx.doi.org/10.1016/0022-2313(93)90021-E.

29. Espinoza VAA, López A, Neumann R, Sosman LP, Pedro SS. Photoluminescence of divalent cobalt ions in tetrahedral sites of zinc orthotitanate. J Alloys Compd. 2017;720:417-22. http://dx.doi.org/10.1016/j.jallcom.2017.05.188.

30. Sosman LP, Abritta T, Pereira AC, Vargas H. Photoacoustic spectroscopy of Co^{2+} in $ZnGa_2O_4$ and $MgGa_2O_4$. Chem Phys Lett. 1994;227(4-5):485-9. http://dx.doi.org/10.1016/0009-2614(94)00856-6.

31. Tanabe Y, Sugano S. On the absorption spectra of complex ions. I. J Phys Soc Jpn. 1954;9(5):753-66. http://dx.doi.org/10.1143/JPSJ.9.753.

32. Henderson B, Bartram RH. Crystal-field engineering of solid-state laser materials. Cambridge Studies in Modern Optics. Cambridge: Cambridge University Press; 2000.

33. Silva EB Jr, López A, Pedro SS, Sosman LP. Photoluminescence of Co^{2+} ions in Mg_2SnO_4 tetrahedral sites. Opt Mater. 2019;95:109202. http://dx.doi.org/10.1016/j.optmat.2019.109202:109202.

Supplementary material

The following online material is available for this article:

Video 1 - Photoluminescence processes.